Nature Communications

https://doi.org/10.1038/s41467-026-70975-2

Article in Press

Noncollinear ferrielectricity in a van der Waals crystal

Received: 23 January 2026

Accepted: 6 March 2026

Cite this article as: Fu, J., Wang, G., Qi, Y. *et al.* Noncollinear ferrielectricity in a van der Waals crystal. *Nat Commun* (2026). https://doi.org/10.1038/s41467-026-70975-2

Jierui Fu, Gang Wang, Yingpeng Qi, Wen He, Yuqiang Fang, Gang Tang, Yanting Peng, Dong Wang, Zhenjie Guan, Xuzhou Sun, Shuming Zhang, Zunyi Deng, Yue Liu, Jiapeng Wang, Songge Li, Tingting Li, Jinjing Zhou, Yuchen Shang, Yankun Yin, Zhaoju Yang, Jinzhong Wang, Yang Ding, Dao Xiang, Liang Zhen, Jiawang Hong, Fuqiang Huang, Junhao Lin, Chengyan Xu & Yang Li

Noncollinear ferrielectricity in a van der Waals crystal

Author Information

Jierui Fu [1,2,†], Gang Wang [3,†] , Yingpeng Qi [4,5,†] , Wen He [1,†] , Yuqiang Fang [6,7,*], Gang Tang [8] , Yanting Peng [8], Dong Wang [9] , Zhenjie Guan [1] , Xuzhou Sun [6] , Shuming Zhang [10] , Zunyi Deng [8] , Yue Liu [1,2] , Jiapeng Wang [1,2] , Songge Li [3] , Tingting Li [3] , Jinjing Zhou [1,2] , Yuchen Shang [11] , Yankun Yin [11] , Zhaoju Yang [10] , Jinzhong Wang [1] , Yang Ding [9] , Dao Xiang [5,7] , Liang Zhen [1,2] , Jiawang Hong [8,*] , Fuqiang Huang [6,7,*] , Junhao Lin [3,12,13,*] , Chengyan Xu [2,14,*] , Yang Li [1,2,*]

Affiliations

1 School of Materials Science and Engineering, Harbin Institute of Technology, Harbin 150001, China

2 MOE Key Laboratory of Micro-Systems and Micro-Structures Manufacturing, Harbin Institute of Technology, Harbin 150080, China

3 State key laboratory of quantum functional materials, Department of Physics and Guangdong Basic Research Center of Excellence for Quantum Science, Southern University of Science and Technology (SUSTech), Shenzhen 518055, China

4 Suzhou Institute for Advanced Research, University of Science and Technology of China, Suzhou 215123, China

5 Key Laboratory for Laser Plasmas (Ministry of Education), School of Physics and Astronomy, Shanghai Jiao Tong University, Shanghai 200240, China

6 Key Laboratory of Intelligent Creation for Extreme Energy Materials (Ministry of Education), School of Materials Science and Engineering, Shanghai Jiao Tong University, Shanghai 200240, China

7 Zhangjiang Institute for Advanced Study (ZIAS), Shanghai Jiao Tong University, Shanghai 201210, China

8 School of Aerospace Engineering, Beijing Institute of Technology, Beijing 100081, China

9 Center for High Pressure Science and Technology Advanced Research, Beijing 100193, China

10 School of Physics, Zhejiang University, Hangzhou 310058, China

11 State Key Laboratory of High Pressure and Superhard Materials, College of Physics, Jilin University, Changchun 130012, China

12 Quantum Science Center of Guangdong-Hong Kong-Macao Greater Bay Area (Guangdong), Shenzhen 518045, China

13 Guangdong Provincial Key Laboratory of Advanced Thermoelectric Materials and Device Physics and Shenzhen Key Laboratory of Advanced Quantum Functional Materials and Devices, Southern University of Science and Technology (SUSTech), Shenzhen 518055, China

14 Sauvage Laboratory for Smart Materials, School of Materials Science and Engineering, Harbin Institute of Technology (Shenzhen), Shenzhen 518055, China

†These authors contributed equally to this work

*Corresponding authors Email:
fangyuqiang@sjtu.edu.cn (Y. Q. Fang);
huangfq@sjtu.edu.cn (F. Q. Huang.);
hongjw@bit.edu.cn (J. W. Hong);
linjh@sustech.edu.cn (J. H. Lin);
cy_xu@hit.edu.cn (C. Y. Xu);
liyang2018@hit.edu.cn (Y. Li)

Abstract

Inspired by noncollinear magnetic dipole order, noncollinear electric dipole order is anticipated to open up rich ferroelectric physics and new opportunities for device applications. However, establishing such order in single crystals remains challenging, as electric polarization is typically locked to crystallographic axes. Here we report noncollinear ferrielectricity in the van der Waals crystal WO_2Br_2, arising from competition between ferroelectric and antiferroelectric phonon modes. The noncollinear dipole order of WO_2Br_2 is revealed by decoupling the antipolar and the polar displacement component, both of which are directly visualized by scanning transmission electron microscopy. This noncollinear dipole order enables 90° polarization flip under hydrostatic pressure through two energetically degenerate transition pathways. Moreover, ultrafast electron diffraction measurements show that optical excitation drives two distinct coherent phonon modes associated with the ferroelectric and antiferroelectric orders. This work clarifies the physics of noncollinear electric dipole order for emergent ferroelectric device applications.

Introduction

Magnetic and electric dipole order underpins functional crystalline materials. Despite distinct origins—magnetic moments from spin and orbital angular momentum, electric dipoles from charge separation—Landau phase theory supplies a unified description of their ordering[1–5]. Classical dipole arrangements manifest as parallel (ferroic), antiparallel (antiferroic), or collinear ferrimagnetic/ferrielectric

configurations[6–10]. Beyond these classical paradigms, angular misalignments enable the noncollinear dipole order, and the magnetic counterpart has been extensively studied in the field of magnetic materials. This magnetic dipole configuration produces exotic spin textures and extraordinary performance such as giant magnetostriction, anomalous Hall effects and spin–orbit torque[11–15], which strongly motivates the exploration of analogous noncollinear electric dipole arrangements for fascinating physics.

Progress toward noncollinear polarization phenomena has been achieved in several systems. For example, in non-Ising ferroelectric domain walls[16–18], artificially designed superlattices[19,20], and twisted-stacked moiré superlattices[21,22], the interplay among electrostatic energy, elastic energy, polarization-gradient energy, and interfacial charge redistribution can stabilize nanoscale noncollinear polarization textures, giving rise to topological polarization structures including polar vortices and polar skyrmions. However, such textures are often closely tied to interfaces and boundary conditions. In such cases, polarization rotation at domain walls is typically confined to a finite region near the wall, whereas topological textures in superlattices depend sensitively on parameters such as the superlattice period, layer thickness, and moiré twist angle. Therefore, constructing an intrinsic, long-range-ordered noncollinear electric dipole order in a single-phase crystal remains an important goal in this field.

Unfortunately, reports of noncollinear dipole order in bulk single crystals remain scarce[23–26], despite the rapid progress in noncollinear electric dipole state achieved through interfacial engineering in superlattices and domain walls. This remains highly challenging because electric polarization is often locked to the crystallographic axes, and lattices with multiple polar axes tend to relax by forming ferroelastic domains rather than stabilizing a single-phase noncollinear dipole ground state[26–28], leaving this field still relatively underexplored.

Recently, noncollinear electric dipole order has been achieved in limited materials via introducing competing interactions or structural instabilities by drawing inspiration from noncollinear magnetics[24–26,29–31]. For instance, the competition between the Bi^{3+} lone pair electrons and the Mn^{3+} Jahn-Teller distortion in $BiCu_xMn_{7-x}O_{12}$ gives rise to an incommensurate helical dipole order[24]. Moreover, Lin et al. reported that the competition between ferroelectric and antiferroelectric modes within a single crystal could yield phonon-frustrated noncollinear electric dipole order, which is the breakthrough in this field

for the search of single-crystal noncollinear ferroelectrics[32]. Owing to its intuitive physical basis, this strategy is considered a promising route for creating noncollinear dipole order.

Van der Waals (vdWs) layered transition-metal oxyhalides, with distorted octahedral coordination that gives rise to diverse polarization phenomena, offer a promising platform for realizing phonon-frustration-induced noncollinear dipoles[33–36]. In the most extensively studied $NbOX_2$ (X = Cl, Br, I), the $4d^1$ electronic configuration of Nb^{4+} drives uniaxial structural distortions through Peierls-type dimerization, which confines the dipole to collinear orientations[37–41]. In contrast, the octahedral distortion of MO_2X_2 (M = Mo, W) is dominated by the directional hybridization between the empty d orbitals of M^{6+} and the anisotropic ligand fields imposed by O^{2-} and X^- anions, promoting richer polarization configurations, including noncollinear arrangements, as has been theoretically demonstrated by Lin et al[32].

Inspired by the pioneering theoretical prediction of phonon-frustrated noncollinear dipole order in monolayer transition-metal dioxydihalides, we revisit this system experimentally. Although their work established a fundamentally new dipolar paradigm, direct experimental evidence has remained elusive, and its impact on polarization switching as well as the tunability of the noncollinear dipole order under external stimuli has yet to be explored.

Here, we unambiguously demonstrate the noncollinear dipole order in vdWs WO_2Br_2 by combining single-crystal X-ray diffraction (SCXRD) for structural resolution, crystallography-targeted scanning transmission electron microscopy (STEM) for direct visualization of W-atom displacements, and theoretical calculations. Moreover, the robust room-temperature in-plane ferroelectricity is revealed via piezoresponse force microscopy (PFM). Impressively, the critical role of noncollinear electric dipoles in polarization switching is revealed through *in-situ* polarization-resolved second harmonic generation (SHG) under hydrostatic pressure, where a 90° polarization rotation is achieved via two energetically near-degenerate transition pathways, involving an intermediate antipolar phase and 45° polar phase respectively. Furthermore, ultrafast structural probing reveals the exotic physics arising from the noncollinear dipole order, as ultrafast electron diffraction (UED) resolves photoexcited coherent phonons associated with the ferroelectric and antiferroelectric orders. These pressure-driven polarization-rotation processes and ultrafast phonon dynamics enable an effective strategy of domain and polarization

engineering for promising ferroelectric memory and high-speed optoelectronic applications.

Results

Visualization of noncollinear atomic displacements in WO_2Br_2

Millimeter-scale, phase-pure WO_2Br_2 crystals were synthesized via a chemical vapor transport (CVT) method (Supplementary Fig. 1a). SCXRD patterns reveal a polar structure belonging to the non-centrosymmetric monoclinic space group *Cc* (No. 9) (Supplementary Table 1). The crystal is composed of two-dimensional [WO_4Br_2] octahedral layers interconnected through corner-sharing oxygen atoms. Halogen atoms (Br) occupy apical sites oriented along the *a*-axis, whereas oxygen atoms reside within the *bc*-plane. As illustrated in Fig. 1a, a mono-unit, defined as one unit-cell (UC) comprised of two atomic layers, exhibits alternating displacements of W atoms toward the upper-left (blue arrows) and lower-left (yellow arrows) along the *c*-axis. The displacements induces noncollinear ferroelectric polarization within the *bc*-plane, giving rise to net polarization along the *c*-axis and antipolar displacement along the *b*-axis. Due to the inherent geometry of the monoclinic crystal system, the stacking axis *a* is inclined relative to the *bc*-plane. Consequently, the W site at fractional coordinates (x, y, z) in 1st UC would coincide with the W site at (x, -y, z+ ½) in 2nd UC if $y = 0$ (i.e., in the absence of a *b*-axis displacement) when projected along the [201] (Figs. 1a, b is the projection along this zone axis) direction. In the actual structure, an antipolar displacement along the *b*-axis leads to $y \neq 0$, breaking the projected overlap and causing a lateral offset between the W atomic columns. Furthermore, W and Br atoms are situated in extremely close proximity along this projection. Both the two factors hamper the intuitive resolution of the noncollinear displacements, as evidenced by experimental observations (Supplementary Fig. 4). Besides, the substantial *Z*-contrast between heavy W ($Z = 74$) and light O ($Z = 8$) further impedes polarization analysis via octahedral core shifts. Therefore, there is not a low-index crystallographic zone axes enable unambiguous resolution of W, Br, and O atomic columns, and meanwhile avoiding stacking-induced imaging artifacts, which is a prerequisite for direct dipole visualization.

To circumvent such constraints, we strategically decoupled the *b*-axis antipolar and *c*-axis polar displacement components through crystallography-targeted analyses, thereby enabling reconstruction of the three-dimensional dipole configuration (Fig. 1d). For quantifying polar displacements along *c*-axis,

relative positional shifts between W and Br atoms within each octahedral cage were determined via atomic-column centroid analysis projected along [010] zone axis. To resolve *b*-axis antipolar order, we employed multi-slice high-angle annular dark-field STEM (HAADF-STEM) simulations, guiding our selection of the [221] zone axis. Although imaging along the [221] direction remains partially constrained by stacking, simulations indicate partial spatial separation of overlapping W and Br atomic columns in few-layer WO_2Br_2 (Supplementary Figs. 5, 6). Additionally, surface-dominated electron scattering in thin specimens further mitigates stacking-induced average effects[42,43], enabling a clear distinction of the antipolar displacements of W atoms along the *b*-axis.

Guided by these insights, aberration-corrected STEM was performed on mechanical-exfoliated samples to directly visualize the atomic displacements. The experimental HAADF image (Fig. 1e) exhibits exceptional agreement with [221] zone-axis simulations, permitting unambiguous identification of antipolar W-atom displacements. The HAADF signal predominantly arises from W columns due to their higher electron scattering cross-section. In this orientation, the low-density atomic column direction corresponds to the *b*-axis, while the high-density direction aligns with the *c*-axis. Within individual layers (corresponding to next-neighbor atom columns), the W displacements along the *b*-axis exhibit a characteristic "↑ ↓ ↑ ↓" antipolar arrangement. For multilayer configurations ($n \geq 2$), the intercalation of lower-layer atoms into the voids of the upper layer results in an "↑↑↓↓↑↑" displacement pattern of W atoms when projected along the [221] zone axis, as shown in the enlarged HAADF image in Fig.1g.

FIB-prepared cross-sectional samples oriented along the [010] axis reveal the ferroelectric displacement component of W-atom displacements, as shown through HAADF imaging in Fig. 1f. The magnified analysis (Fig. 1h) highlights pronounced deviations of the W columns from the centroid of the Br-anion plane along the *c*-axis direction, as indicated by the arrow vectors (magnified by a factor of five relative to their actual displacement). Statistical quantification (Fig. 1i) confirms alternating ±0.23 Å displacements along *b*-axis, concurrent with net polarization along *c*-axis, with an average displacement of 0.27 Å, conclusively establishing coexisting antipolar and polar displacement along *b*-axis and *c*-axis respectively. These atomic displacements are not confined to a local region: large-area HAADF imaging also reveals uniformly distributed polar and antipolar displacements, demonstrating that the noncollinear

dipole order exhibits long-range order (Supplementary Figs. 9, 10). Differential phase contrast (DPC) imaging, together with DPC simulations based on ion scattering factors (Fig. 1j and Supplementary Fig. 11), reveals asymmetric atomic-scale electric field distributions induced by ferroelectric polarization, with the asymmetry being most pronounced at the W atomic columns, in agreement with previous reports[44,45]. The local electric fields probed by DPC, which reflect polarization-induced charge redistribution and the associated projected electric-field gradients, when combined with the leftward polar displacement of the W atomic columns observed in HAADF-STEM images, provide further validation of the ferroelectric order along the *c*-axis. The spatial superposition of antipolar and polar dipole configurations results in the noncollinear dipole arrangement in WO_2Br_2.

Robust room-temperature in-plane ferroelectricity in WO_2Br_2

STEM characterizations directly resolve noncollinear displacements of W atoms, and first-principles calculations were employed to elucidate the underlying mechanism governing this unique dipole order. Based on the experimentally resolved WO_2Br_2 structure, our theoretical prediction identifies a high-symmetry paraelectric phase crystallizing in the *C2/m* space group. Phonon dispersion analysis of the paraelectric phase reveals prominent imaginary frequencies, confirming an intrinsic structural instability, as illustrated in Supplementary Fig. 12. Notably, a Γ-point phonon mode with B_u symmetry induces polar displacements (ferroelectric order, FE) along the *c*-axis, while a B_g mode at the *A* point drives antipolar distortion (antiferroelectric order, AFE) along the *b*-axis. In addition, the DFT energy profiles for the Γ_2^- (FE), A_2^+ (AFE), and combined $\Gamma_2^- + A_2^+$ distortions show that the mixed FE+AFE distortion corresponding to the noncollinear state has a significantly lower energy minimum than either the FE-only or AFE-only structure (Supplementary Fig. 13). This indicates that, although each distortion mode individually exhibits dynamical instability, their cooperative interaction stabilizes a noncollinear ferrielectric configuration, in agreement with experimental observations. In WO_2Br_2, the resultant staggered (antipolar) dipole component alternates along the *b*-axis, while a net polar component survives along the *c*-axis, yielding a macroscopic polarization along *c*-axis.

According to theoretical calculations above, where a noncollinear arrangement of local electric dipoles gives rise to in-plane ferroelectricity, we then performed PFM measurements on mechanically exfoliated

WO_2Br_2 flakes transferred onto Au-coated SiO_2/Si substrates, with the topography of the characterized region shown in Fig. 2a. The in-plane PFM amplitude and phase images (Figs. 2b, c) clearly reveal 180° domain structures independent of the AFM morphology, in which adjacent domains exhibit comparable amplitudes together with a 180° phase contrast, and the domain walls appear as lines of reduced amplitude. To further confirm ferroelectric domain switching, we conducted point-by-point polarization-reversal measurements and recorded PFM hysteresis loops (Figs. 2d, e), in which the in-plane phase displays an approximately 180° counter-clockwise switching hysteresis and the amplitude exhibits the characteristic butterfly loop, while loops measured on the bare substrate show no hysteresis (Supplementary Fig. 15), ruling out instrumental artifacts. A visualization of the field-induced polarization reversal behavior is shown in Figs. 2f–i. When positive or negative single-point bias is applied along the appropriate direction, the written domains exhibit a phase shift of approximately 180° relative to the surrounding region (Supplementary Fig 19). A full sequence of domain writing and erasing is provided in Supplementary Fig 20. The in-plane nature of the polarization is further verified by rotating the relative angle between the probe and the sample (Supplementary Figs. 22), from which the PFM amplitude reaches a maximum when the polarization direction is perpendicular to the scan direction, decreases progressively upon rotation, and nearly vanishes when the polarization becomes parallel to the scan.

Re-orientation of polar axis in WO_2Br_2 under hydrostatic pressure

Given that WO_2Br_2 crystallizes in the non-centrosymmetric space group *Cc*, with structural asymmetry enabling the generation of measurable second-order nonlinear optical susceptibility, we then evaluate its second-harmonic generation (SHG) behavior for identification of crystalline orientations. Fig. 3a shows the optical image of a ~50 nm-thick WO_2Br_2 flake (white region), and the power-dependent SHG spectra (Supplementary Figs. 25, 26) suggests a quadratic dependence of SHG intensity on incident power, confirming the second-order nonlinearity. According to the power-dependent SHG measurements of WO_2Br_2 and referenced $NbOI_2$, monolayer-equivalent WO_2Br_2 possesses a second-order nonlinear susceptibility $\chi^{(2)}$ of ~120 pm/V, (Supplementary Note 2), which is comparable to top-tier 2D nonlinear optical materials such as $NbOI_2$ and $NbOCl_2$[39,46]. The strong nonlinearity, coupled with persistent symmetry breaking, enables direct optical visualization of SHG signals of WO_2Br_2: 1040 nm laser

excitation with power of 35 μW on WO_2Br_2 flake generates a visible 520 nm emission (17 nW output, conversion efficiency ~0.05%), as shown in Fig. 3b, demonstrating exceptional nonlinear conversion capabilities.

We then analyze the SHG polarization behavior of WO_2Br_2. Under the overall configuration, the polarization-dependent SHG intensity polar plot (Fig. 3c) displays a two-lobe pattern, where the lobe central axis coincides with the spontaneous polarization *c*-axis (Supplementary Fig 24), suggest that the maximum SHG response is generated when the polarization direction of pump light aligns with the *c*-axis (referred to the polar axis), donated as **E**//*c*, while the minimum SHG response is generated when **E**//*b* (referred to the nonpolar axis), which stems from the inherently 90° angular difference between the *b*-axis and *c*-axis stipulated by the monoclinic crystal structure of WO_2Br_2. This anisotropy persists under the parallel polarization configurations, while a four-lobe profiles with intensity maxima oriented at 45° relative to the crystallographic axes generated under the perpendicular configuration (Fig. 3c and Supplementary Fig 24). The high SHG efficiency and the in-plane SHG anisotropy of WO_2Br_2 enables precise identification of crystallographic axes.

According to our theoretical calculations, WO_2Br_2 is capable of undergoing a 90° polarization reorientation. Crucially, the noncollinear dipole order gives rise to nontrivial polarization-switching behavior, manifested as two nearly energy-degenerate transition pathways that proceed via distinct intermediate states, which will be discussed in the following sections. However, experimental attempts to induce this re-orientation through external electric fields (23.1 kV/cm) and uniaxial strain application along the *b*-axis (achieved via flexible substrate bending with 1.6% strain) in WO_2Br_2 both failed, where the crystal orientation was not changed (Supplementary Figs. 29, 30), indicating prohibitively high energy barriers in this interchange process between *b*- and *c*-axes. As an alternative approach, hydrostatic pressure through a diamond anvil cell (DAC) can generate gigapascal-scale stresses that induces bulk lattice deformations unattainable through conventional methods. As shown in Fig. 3d, pressure-dependent crystallographic orientation evolution in WO_2Br_2 was investigated under hydrostatic compression using DAC, with complete experimental details provided in the Methods section.

To mitigate anisotropic deformation caused by adhesion forces between the sample and diamond anvils

that could compromise hydrostatic conditions[47], we selected WO_2Br_2 flakes with a relatively large thickness (~100 nm) for high-pressure experiments. Optical images and polarization-resolved SHG polar plots acquired from the same location of the sample under ambient pressure (A.P.) and 6.0 GPa are presented in Supplementary Fig. 31, where 0° in SHG polar plots corresponds to the *x*-axis of the laboratory coordinate system. A distinct 90° reorientation is observed, where the angle of maximum SHG intensity shifts from ~46.5° (A.P.) to ~136.5° (6.0 GPa) while maintaining comparable signal intensity, eliminating the orientation ambiguity induced by SHG intensity variations. The observed rotation of SHG polar plots therefore directly demonstrates pressure-induced interchange of the *b*-axis and *c*-axis, exhibiting characteristics analogous to interconversion of ferroelastic variants. *In-situ* SHG intensity mapping of the sample under the configurations of both **E**//*c* and **E**//*b* revealed progressive orientation transitions under pressure, as shown in Figs. 3e-h. At ambient pressure, SHG signal across the sample exhibits uniform distribution, confirming a homogeneous single-orientation, where the SHG intensity under **E**//*c* is significantly stronger than under that **E**//*b* configuration. Under compression of 6.0 GPa, from the SHG intensity mapping with **E**// *c*, the intensity of certain locations decreases with inhomogeneous distribution, while the intensity of corresponding locations increases under **E**// *b*, providing direct evidence of reorientation of crystalline polar and nonpolar axis.

To reveal the underlying mechanism of pressure-driven reorientation of crystal axes in WO_2Br_2, we then carried out the first-principles calculations to evaluate the potential transition pathways. Using the climbing image nudged elastic band (CI-NEB) method, two energetically favorable transition pathways are identified (Figs. 4a, b), which exhibit double-barrier features due to the existence of metastable phases: (1) the antipolar (AP) phase pathway corresponding to metastable structures with antiparallel local dipoles along diagonal directions of [WO_4Br_2] octahedra, and (2) the 45° collinearly polar phase pathway (45° CP) corresponding to intermediate states with the local dipoles along identical directions, resulting in net polarization oriented at 45° relative to the initial net polarization direction. The AP and 45° CP pathway show near-degeneracy with energy barriers of 5.7 and 5.8 meV per atom respectively. Additional simulations based on the collinear dipole model (Supplementary Fig. 34) demonstrate that these nearly degenerate double-barrier energy pathways are unique features for noncollinear dipole orders. In Fig. 4b,

the evolution of SHG polar plots reveals significant differences between the two pathways: SHG signals of the intermediate phase for AP path vanish due to centrosymmetric structure, while the central axis of petals in 45° CP path gradually rotates from 0° through 45° to 90° in synchronization with polarization direction changes. The energy barriers of both AP and 45° CP paths decline to the half as the compression increases to 1% (Fig. 4c), confirming the preferential pressure-driven orientation transition.

To elucidate the pressure-induced reorientation process, we conducted polarization-dependent SHG measurements at selected sample locations under varying pressures (Figs. 4d–g). Fig. 4d presents the evolution of SHG intensity with pressure along the directions of **E**//*c* (polar axis) and **E**//*b* (nonpolar axis). At ambient pressure, the SHG intensity measured along the polar axis is ~31 times higher than that along the nonpolar axis. Upon increasing the pressure to 1.1 GPa, the polar-axis SHG intensity drops sharply, whereas the nonpolar-axis intensity shows a slight increase. As a result, at 1.1 GPa the nonpolar-axis intensity becomes dominant, exceeding the polar-axis intensity by a factor of ~5. It should be noted that although the second-harmonic generation (SHG) response of a centrosymmetric antipolar phase is theoretically zero, the experimental observations reveal significant SHG intensity reduction in localized regions rather than complete disappearance (Supplementary Fig. 32). This can be attributed to two factors: (1) spatial inhomogeneity during the high-pressure phase transition, as evidenced by SHG mapping in Figs. 3e-h, and (2) limitations of the imaging system, where the use of low-NA objective lenses, which is necessary to satisfy working distance constraints, results in a relatively large laser spot size. Beyond 3.0 GPa, the SHG intensity gradually recovers, while the nonpolar axis response reaching nearly the same level as at ambient pressure by 6.0 GPa. Remarkably, beyond 1.1 GPa, the SHG signal along the nonpolar axis consistently remains stronger than that along the polar axis throughout the entire pressure range, and the SHG responses reach to 1:24 along polar and nonpolar axis under 6.0 GPa, indicating that the initial nonpolar *b*-axis became polar *c*-axis under pressure.

Fig. 4e displays SHG polar plots at representative pressures of ambient pressure, 2.4 GPa, and 6.0 GPa in Fig. 4d, corresponding to the initial, the ongoing transition, and the fully reoriented state respectively. The characteristic two-lobed SHG pattern undergoes an angular rotation of about 90° as the pressure increases from ambient to 6.0 GPa, in excellent agreement with the theoretical prediction. These results

reveal the emergence of an intermediate phase in which the SHG intensity is strongly suppressed, and consistent with a nearly vanishing macroscopic polarization, which corresponds to the AP pathway predicted by theoretical calculations.

Moreover, our experiments revealed another distinct transition pathway. Fig. 4f displays the evolution of SHG intensity along the polar and nonpolar axes throughout this transition. Although SHG attenuation is also observed below 6.0 GPa, the SHG intensity along the polar axis consistently remains stronger than that along the nonpolar axis, indicating the absence of polarization reorientation. Interestingly, at 6.0 GPa, the SHG intensities along both polar and nonpolar directions reach nearly the same level. Beyond this pressure, the intensity along polar axis decreases significantly relative to the nonpolar axis, signaling the completion of reorientation. SHG polar plots shown in Fig. 4g offer a clearer visualization of this process. At 6.0 GPa, an anomalous SHG polar plot with preserved two-lobe symmetry is observed, wherein the polar axis rotates by ~45° while maintaining substantial signal strength. This indicates the emergence of a polar intermediate phase, distinct from the centrosymmetric phase along the AP pathway. Upon 7.3 GPa, the polar axis undergoes an ~90° rotation from the angle under ambient pressure, confirming a full switching of the crystal axes. The intermediate phase maintains polar symmetry with a 45°-rotation of polar axis, in agreement with theoretically predicted 45° CP pathway. Notably, this intermediate phase exhibits enhanced SHG intensity along its own nonpolar direction (~0°) compared to pristine WO_2Br_2, consistent with theoretical predictions presented in Fig. 4b.

The coexistence of these two nearly degenerate transition pathways, differing by only ~0.1 meV/atom, substantiates the predicted near-degenerate energy landscape for noncollinear dipole systems and provides critical role of noncollinear dipole order during the polarization switching process. These transition paths in WO_2Br_2 are strongly different from the case in conventional ferroelectrics such as HfO_2[48,49], where the 180°/90° polarization reversal in WO_2Br_2 does not require 180°/90° rotation of every local dipole[32]. Instead, polarization reversal can be driven through coordinated local dipole rotation across neighboring units, which constitutes a distinctive characteristic of noncollinear ferrielectricity. The coordinated behavior enables multiple switching pathways emerge during 90° polarization rotation depending on different metastable intermediate structures. Notably, the metastable phases in WO_2Br_2 remain stable over

a relatively wide pressure range, enabling the coexistence and interconversion of multiple polarization states (as shown in Fig. 4a), which offers promising potential for applications in information storage devices.

After clarifying the two transition pathways of WO_2Br_2 under compression, we further investigated how the crystal structure evolves along these pathways. Raman spectroscopy serves as a sensitive probe for tracking structural evolution under hydrostatic pressure. Taking the AP transition pathway as an example, we performed *in-situ* Raman spectra measurements to reveal the high-pressure structural evolution of WO_2Br_2 (Supplementary Fig. 40). The results show that the original vibrational modes are preserved throughout compression, while novel emerging Raman modes appear at the early stage under pressure and disappear at higher pressures. Consequently, the Raman spectra obtained at 6.0 GPa closely resembles that at ambient pressure.

Further analysis of the pressure-dependent frequencies of different vibrational modes reveals that the out-of-plane vibrational mode (A'_3) exhibits a monotonic blueshift with increasing pressure, while the in-plane vibrational modes (A'_1, A'_2, A'_4) show redshift in the low-pressure region (<3.0 GPa) and blueshift at higher pressures (>3.0 GPa) (Supplementary Fig. 41). The redshift of the in-plane modes at low pressure indicates in-plane bond softening or lattice expansion[50,51], consistent with the emergence of an antipolar intermediate phase. With further compression, the in-plane modes switch from redshift to blueshift, indicating the recovery of conventional pressure-induced bond stiffening and suggesting that the structure ultimately stabilizes into a noncollinear dipolar configuration. The formation of this metastable intermediate phase is mainly governed by in-plane atomic rearrangements, in agreement with the theoretically predicted transition pathway.

Consistent with the Raman spectra results, *in-situ* powder and single-crystal XRD under hydrostatic pressure (Supplementary Figs 35-42, Supplementary Table 5) indicate that, although WO_2Br_2 undergoes a space-group change (*Cc* to *Pcc2*) at 5.0 GPa, the transition does not involve a drastic structural reconstruction but rather a gradual, moderate evolution of the lattice. Taken together with the Raman and XRD analyses, WO_2Br_2 can still retain a noncollinear dipole configuration to a certain extent under hydrostatic pressure.

FE and AFE coherent phonon dynamics in WO_2Br_2

In WO_2Br_2, the presence of ferroelectric and antiferroelectric soft phonon modes in the high-symmetry paraelectric phase drives polar displacements of W atoms along the *c*-axis and antipolar displacements along the *b*-axis, which together give rise to a noncollinear electric dipole order. This particular noncollinear dipole order in WO_2Br_2 provides an ideal platform for coherent control of the polar and antipolar orders separately or simultaneously. Here, we identify this concept by the combination of Raman spectra, DFT simulation and ultrafast electron diffraction (UED). The static Raman spectra in Fig. 5b displays the two *A′* phonon modes with the frequnecy of 2.83 THz and 3.70 THz. The atomic movements and vibrational frequencies of these two phonon modes acquired by DFT simulation are shown in Figs. 5c and d. For the 2.70 THz phonon mode (i.e., *A′*(FE)), the collective in-phase vibration of W atoms along the *c*-axis together with their opposite motion relative to Br atoms along the same axis, indicates that this mode primarily modulates the ferroelectric order. In contrast, for the 3.70 THz mode, W and Br atoms vibrate out of phase along the *b*-axis; however, neighboring chains of W atoms oscillate in opposite directions along *b*-axis, demonstrating that this mode mainly modulates the antiferroelectric order (i.e., *A′*(AFE)). Polarization-resolved Raman spectra also reveal that these two *A′* modes exhibit a phase difference close to 90° (Supplementary Figs. 42c, d), which further supports that they are associated with the polar and nonpolar axes respectively.

With femtosecond laser pump, we monitor the coherent phonon modes by the intensity change of Bragg reflections. Both the *A′*(FE) and *A′*(AFE) phonon mode are coherently excited as shown in Figs. 5e-f and Figs. 5g-h (Supplementary Fig 48). The long lifetime of these coherent phonon modes indicates the primary ferroelectric and antiferroelectric modes. Therefore, the concept of coherent control of the ferroelectric and antiferroelectric dipole orders separately and simultaneously, which is the unique feature of noncollinear ferroelectricity of WO_2Br_2, has been identified. This coherent excitation regime sheds light on the ultrafast control of the exotic physics in noncollinear ferroelectricity, such as the dipole-based skyrmions[32], for applications in high-speed optoelectronic devices[52]. Such experimental explorations toward ultrafast switching of macroscopic orders[32,53,54] and metastable states[55–57] are expected.

In summary, we have theoretically and experimentally established the phonon-frustration driven

noncollinear electric dipole order and room-temperature ferroelectricity in the layered crystal WO_2Br_2. Hydrostatic pressure enables a nontrivial crystal axes 90° switching, and ultrafast structural probes reveal the distinctive coherent phonon dynamics associated with the noncollinear dipole state. Atomic-scale HAADF-STEM microscopy directly visualized the antipolar W atoms arrangement along the *b*-axis and polar alignment along the *c*-axis. PFM measurements and hysteresis loops confirmed macroscopic ferroelectric properties. Under hydrostatic compression, WO_2Br_2 exhibits coexistence of two distinct pathways during 90° polarization switching: one involving intermediate phases with vanishing polarity and another maintaining polarity with 45°-rotation of polar axis relative to the pristine state, which is the direct consequence of noncollinear dipole order in WO_2Br_2. This pressure-driven 90° rotation further offers an effective route for domain and domain-wall engineering. Ultrafast electron diffraction measurements additionally demonstrate excitation of coherent phonon modes associated with ferroelectric and antiferroelectric modes upon photoexcitation. This work deepens the understanding of noncollinear ferroelectric physics and opens a practical pathway for polarization-state control and domain engineering in ferroelectric memory devices.

Methods

Materials synthesis

High-purity WO_2Br_2 single crystals were synthesized through CVT method. The chemical reactants W, WO_3 and Br_2 were thoroughly mixed in a molar ratio of 1:2:6 and sealed into an evacuated quartz tube (10^{-5} torr). The tubes were heated in a two-zone furnace, and the reaction region and crystal growth region were kept at 450 ℃ and 300 ℃ for 5 days, respectively. Finally, the reddish-brown plate-like crystals can be obtained at the growth region.

Structure characterizations

Single-crystal X-ray diffraction was performed on a Bruker D8 QUEST diffractometer equipped with Mo *Kα* radiation. The diffraction data were collected at room temperature by the *ω*- and *φ*-scan methods. The crystal structure was solved and refined using APEX3 program. Absorption corrections were performed using the multi-scan method (SADABS). The atomic structure is visualized using the VESTA software[58]. The samples for STEM characterization were prepared via mechanical exfoliation and dry

transfer. WO_2Br_2 crystals were first exfoliated using 3M Scotch tape to expose cleavage planes, followed by picking up the exfoliated flakes with a polydimethylsiloxane (PDMS) film to obtain nanosheets. The thickness of the nanosheets was pre-screened via optical microscope (BX53M, Olympus) to select suitable samples. For in-plane STEM observation, selected nanosheets were transferred onto porous silicon nitride TEM grids using standard dry transfer methods. For cross-sectional observation, nanosheets were initially transferred onto SiO_2/Si substrates. After determining their crystallographic orientation via polarization-dependent SHG, thin lamellae were milled using a focused ion beam-scanning electron microscopy (FIB-SEM) system via a standard lift-out process, transferred onto TEM grids, and polished to electron transparency. HAADF-STEM and DPC imaging were performed using a probe-corrected JEOL ARM-200F TEM (200 kV) for in-plane specimens and an FEI Titan Themis G2 double-aberration-corrected TEM (300 kV) for cross-sectional specimens. For basal-plane imaging, a collection angle of 68-200 mrad and a convergence semiangle of 29.2 mrad were employed. Cross-sectional characterization utilized a collection angle of 52-200 mrad and a convergence semiangle of 25 mrad. Beam current was maintained below 30 pA for all experiments to minimize radiation damage. Electron diffraction patterns were simulated using the software *Recipro*[59], while multi-slice STEM images were generated using QSTEM[60].

Extraction of atomic displacements and vector mapping

Polar atomic displacements in WO_2Br_2 along the [010] direction were quantified using a custom Python workflow based on template matching. Initial templates for W, Br1, and Br2 motifs were selected as 50×50-pixel windows from the HAADF-STEM image (Supplementary Fig. 10a). To reduce noise, each template was refined by averaging high cross-correlation regions, producing noise-reduced reference patterns. These templates were used for normalized cross-correlation across the entire image to obtain initial atomic coordinates. Sub-pixel accuracy was achieved by refining atomic positions using two-dimensional Gaussian peak fitting. The polar displacement vector for each unit cell was calculated as the offset of the W atom relative to the midpoint of its surrounding Br atoms, representing the local polar distortion. The resulting displacement field was visualized by overlaying arrow vectors magnified by a factor of five (Supplementary Fig. 10b). For WO_2Br_2 imaged along the [221] direction, antipolar displacements were extracted using the CalAtom software[61]. Atomic coordinates (Fig. 1e) were identified

by applying an intensity threshold to locate atomic maxima, followed by sub-pixel localization using center-of-mass calculations. The mean *y*-coordinate of each atomic row was taken as the local reference center, and atomic displacements were computed relative to this reference. The column-averaged antipolar shift for each atomic column was obtained by averaging these displacements, forming a single data point in Fig. 1i.

PFM measurements

The exfoliated crystals were directly transferred onto SiO_2/Si substrates coated with a 50 nm gold film for PFM characterization. PFM images were acquired in contact mode using a Bruker Dimension Icon atomic force microscope. Measurements were performed with a platinum/iridium-coated silicon tip (SCM-PIT, Bruker) with a radius of 20 nm and a spring constant of ~3.0 N m^{-1}. The driving frequency and amplitude for PFM imaging were set to the in-plane contact resonance frequency (~760 kHz) and 2000 mV, respectively. PFM switching spectroscopy was conducted by applying a triangular-wave voltage (±6 V) to the tip while monitoring the PFM phase and amplitude under a 2000 mV drive voltage.

Optical characterization

SHG and Raman spectroscopy measurements were performed using a custom-built spectroscopic system (detailed in Supplementary Fig. 23). The SHG signal was excited by a 1034-nm fibre-based femtosecond laser (Femto-10, Huaray), with its polarization purified via a Glan-Thompson prism (GTP-10, LBTEK). Polarization-resolved SHG spectroscopy employed a shared half-wave plate configuration[62]: an achromatic half-wave plate (SAHWP05M-700, Thorlabs) rotated the polarization of both the incident laser and the emitted signal. Switching between parallel and perpendicular polarization configurations was achieved by adjusting the angle of a polarizer in the signal collection path. The SHG signal was collected using a spectrometer (Shamrock 500i, Andor). For Raman spectroscopy, a 523-nm laser (Samba 04-01, Cobolt) was used as the excitation source. The laser beam was purified and filtered using a Bragg bandpass filter (BPF-532, OptiGrate) and two notch filter (BNF-532, OptiGrate) to resolve Raman peaks across low-to-high wavenumber regions.

Hydrostatic pressure measurements

For spectroscopic measurements, appropriately sized samples were transferred onto the surface of a DAC via a dry transfer method. During *in-situ* single crystal and powder XRD testing, single-crystal samples or fine powders were selectively sieved for optimal particle size, and loaded into the high-pressure chamber using a microtip. The high-pressure chamber was sealed with a stainless-steel gasket containing a central aperture of 120 μm, while low-fluorescence silicone oil served as the pressure-transmitting medium. Ruby particles with diameters ranging from 10–20 μm were precisely positioned within the DAC using a microtip for subsequent pressure calibration. Unit cell parameter refinements were performed using the GSAS II software[63].

In millimetre-scale sample high-pressure experiments, WO_2Br_2 flakes were stacked within a cylindrical platinum sample chamber prior to hermetic sealing. High-pressure experiments were performed by ultrahard tungsten carbide anvils assembly in a 10 MN Walker-type LVP (the State Key Laboratory of Superhard Materials, Jilin University). The pressure was increased to 8.0 GPa first over around 30 h, and then released slowly over the course of approximately 30 h.

DFT calculations

Density functional theory (DFT) calculations were performed by Vienna ab initio Simulation Package (VASP)[64] and a plane-wave pseudopotential code, QUANTUM ESPRESSO[65]. The exchange-correlation function was Perdew–Burke–Ernzerhof (PBE) generalized gradient approximation (GGA)[66]. Optimized norm-conserving pseudopotentials were adopted to treat the electron-ion interactions. In the geometry optimization and self-consistent field calculations of monolayer WO_2Br_2, the plane-wave kinetic energy cut-off was 140 Ry and the k-point mesh was 4×8×1. A convergence threshold of 10^{-10} Ry was used for the self-consistent cycle. The convergence thresholds of energy and force for the structural relaxation were 10^{-6} Ry/Bohr and 10^{-5} Ry/Bohr, respectively. The computed in-plane lattice parameters are 7.6 and 3.9 Å, matching well with the experimental structure (7.7 and 3.9 Å). The SHG susceptibility was calculated using a denser k-point mesh of 12×24×1 and 280 bands (including 80 valence bands) for convergence[67]. Spin-orbit coupling (SOC) effects were incorporated into the theoretical modelling of SHG. CI-NEB calculations for 1×2×1 supercell was performed using 9 images to obtain the transition path with the minimum energy and saddle points. Limited by the restriction of lattice relaxation using the

CI-NEB method, the lattice parameter of the supercell was fixed to the average of two in-plane lattices, which is 7.7 Å. The k-point mesh was set to 4×4×1 accordingly. A blueshift of bandgap about 0.14 eV due to the lattice parameter modulation is considered in the computed SHG polar plots in Fig. 4. The phonons were computed by the density functional perturbation theory (DFPT)[68].

UED characterization

For the MeV femtosecond electron diffraction system, the 400 nm, 30 fs and 400 Hz laser pulse (Vitara and Legend Elite Duo HE, Coherent) is split into the pump and the probe pulse. The pump pulse excites the sample and the probe pulse is frequency tripled in nonlinear crystals before illuminating a photocathode for electron pulse generation. After being accelerated by an intense radio-frequency field to relativistic velocity (~0.989c), the electron pulse goes through a double-bend achromatic lens for pulse compression and jitter removal. The spot size of the electron pulse on the sample is ~150 μm FWHM, around five times smaller than the size of the pump laser, ensuring a homogeneous photoexcitation. The diffraction pattern is imaged by a phosphor screen (P43) and recorded by an electron-multiplying charge-coupled device (Andor iXon Ultra 888). The overall temporal resolution of the MeV UED system is ~50 fs. Further details for the system can be found in our previous work[69]. Single crystal WO_2Br_2 nanofilms are prepared via mechanical exfoliation from the bulk crystal and transferred to TEM Si_3N_4 windows for femtosecond electron diffraction experiments. The samples with the thickness of ~ 30 nm are characterized by optical microscopy and TEM.

Data Availability

The data generated in this study are provided in the main text, supplementary information, and source data file. Additional data are available from the corresponding author on request. Source data are provided with this paper.

References

1. Landau, L. The theory of phase transitions. *Nature* **138**, 840–841 (1936).
2. Landau, L. & Lifshitz, E. On the theory of the dispersion of magnetic permeability in ferromagnetic bodies. in *Perspectives in theoretical physics* (ed. Pitaevski, L. P.) 51–65 (Pergamon, Amsterdam,

1992).

3. Devonshire, A. F. XCVI. Theory of barium titanate: part I. *Lond. Edinb. Dublin Philos. Mag. J. Sci.* **40**, 1040–1063 (1949).
4. Dong, S., Liu, J.-M., Cheong, S.-W. & Ren, Z. Multiferroic materials and magnetoelectric physics: symmetry, entanglement, excitation, and topology. *Adv. Phys.* 0–120 (2015).
5. Lee, J. H. *et al.* A strong ferroelectric ferromagnet created by means of spin–lattice coupling. *Nature* **466**, 954–958 (2010).
6. Song, C. *et al*. Altermagnets as a new class of functional materials. *Nat. Rev. Mater.* 1–13 (2025).
7. Xie, Y. *et al.* Emerging ferromagnetic materials for electrical spin injection: towards semiconductor spintronics. *npj Spintron.* **3**, 1–16 (2025).
8. Jang, J. *et al.* Sub-unit-cell-segmented ferroelectricity in brownmillerite oxides by phonon decoupling. *Nat. Mater.* 1–8 (2025).
9. Si, Y. *et al.* Ideal antiferroelectricity with large digital electrostrain in $PbZrO_3$ epitaxial thin films. *Nat. Commun.* **16**, 4263 (2025).
10. Zhou, Z. *et al.* Manipulation of the altermagnetic order in CrSb via crystal symmetry. *Nature* **638**, 645–650 (2025).
11. Rimmler, B. H., Pal, B. & Parkin, S. S. P. Non-collinear antiferromagnetic spintronics. *Nat. Rev. Mater.* **10**, 109–127 (2025).
12. Ye, L. *et al.* Hopping frustration-induced flat band and strange metallicity in a kagome metal. *Nat. Phys.* **20**, 610–614 (2024).
13. Deng, S. *et al.* Phase transitions associated with magnetic-field induced topological orbital momenta in a non-collinear antiferromagnet. *Nat. Commun.* **15**, 822–830 (2024).
14. Govinden, V. *et al.* Spherical ferroelectric solitons. *Nat. Mater.* **22**, 553–561 (2023).
15. Chai, Y.-S. *et al.* Giant magnetostriction and nonsaturating electric polarization up to 60 T in the polar magnet $CaBaCo_4O_7$. *Phys. Rev. B* **103**, 174433 (2021).
16. Wei, X.-K. *et al.* Néel-like domain walls in ferroelectric $Pb(Zr,Ti)O_3$ single crystals. *Nat. Commun.* **7**, 12385 (2016).

17. Cherifi-Hertel, S. *et al.* Non-ising and chiral ferroelectric domain walls revealed by nonlinear optical microscopy. *Nat. Commun.* **8**, 15768 (2017).
18. Li, Y. *et al.* Unusual topological polar texture in moiré ferroelectrics. *Nat. Commun.* **16**, 5451 (2025).
19. Das, S. *et al.* Observation of room-temperature polar skyrmions. *Nature* **568**, 368–372 (2019).
20. Yadav, A. K. *et al.* Observation of polar vortices in oxide superlattices. *Nature* **530**, 198–201 (2016).
21. Tsang, C. S. *et al.* Polar and quasicrystal vortex observed in twisted-bilayer molybdenum disulfide. *Science* **386**, 198–205 (2024).
22. Sánchez-Santolino, G. *et al.* A 2D ferroelectric vortex pattern in twisted $BaTiO_3$ freestanding layers. *Nature* **626**, 529–534 (2024).
23. Zheng, W. Skyrmion nanodomains in ferroelectric–antiferroelectric solid solutions. *Nat. Mater.* 0–21 (2025).
24. Khalyavin, D. D. *et al.* Emergent helical texture of electric dipoles. *Science* **369**, 680–684 (2020).
25. Gao, B. *et al.* An intriguing canting dipole configuration and its evolution under an electric field in La-doped Pb(Zr,Sn,Ti)O_3 perovskites. *Microstructures* **2**, 2022010 (2022).
26. Wang, N. *et al.* Noncollinear ferroelectric and screw-type antiferroelectric phases in a metal-free hybrid molecular crystal. *Nat. Commun.* **15**, 10262 (2024).
27. Damodaran, A. R. *et al.* New modalities of strain-control of ferroelectric thin films. *J. Phys.: Condens. Matter* 37–75 (2016).
28. Yu, Z., Guo, R. & Bhalla, A. S. Orientation dependence of the ferroelectric and piezoelectric behavior of Ba(Ti1-xZrx)O3 single crystals. *Appl. Phys. Lett.* **77**, 1535–1537 (2000).
29. Zhao, H. J., Chen, P., Prosandeev, S., Artyukhin, S. & Bellaiche, L. Dzyaloshinskii–moriya-like interaction in ferroelectrics and antiferroelectrics. *Nat. Mater.* **20**, 341–345 (2021).
30. Fabini, D. H. *et al.* Noncollinear electric dipoles in a polar chiral phase of CsSnBr3 perovskite. *J. Am. Chem. Soc.* **146**, 15701–15717 (2024).
31. Yang, X., Chen, J., Wang, S.-S. & Dong, S. Noncollinear ferrielectricity and hydrogen-induced ferromagnetic polar half-metallicity in MnO_3Cl. *Phys. Rev. B* **110**, 134113 (2024).
32. Lin, L.-F., Zhang, Y., Moreo, A., Dagotto, E. & Dong, S. Frustrated dipole order induces noncollinear

proper ferrielectricity in two dimensions. *Phys. Rev. Lett.* **123**, 067601 (2019).

33. Chu, J. *et al.* 2D polarized materials: ferromagnetic, ferrovalley, ferroelectric materials, and related heterostructures. *Adv. Mater.* **33**, 2004469 (2021).
34. Zhang, D., Schoenherr, P., Sharma, P. & Seidel, J. Ferroelectric order in van der waals layered materials. *Nat. Rev. Mater.* 1–16 (2022).
35. Wang, C., You, L., Cobden, D. & Wang, J. Towards two-dimensional van der waals ferroelectrics. *Nat. Mater.* 1–11 (2023).
36. Li, S. *et al.* Van der waals ferroelectrics: theories, materials, and device applications. *Adv. Mater.* **36**, 2301472 (2024).
37. Jia, Y., Zhao, M., Gou, G., Zeng, X. C. & Li, J. Niobium oxide dihalides NbOX2: a new family of two-dimensional van der waals layered materials with intrinsic ferroelectricity and antiferroelectricity. *Nanoscale Horiz.* **4**, 1113–1123 (2019).
38. Fang, Y., Wang, F., Wang, R., Zhai, T. & Huang, F. 2D $NbOI_2$: a chiral semiconductor with highly in-plane anisotropic electrical and optical properties. *Adv. Mater.* **33**, 2101505 (2021).
39. Guo, Q. *et al.* Ultrathin quantum light source with van der waals $NbOCl_2$ crystal. *Nature* **613**, 53–59 (2023).
40. Wu, Y. *et al.* Data-driven discovery of high performance layered van der waals piezoelectric $NbOI_2$. *Nat. Commun.* **13**, 1884 (2022).
41. Guo, Q. *et al.* Colossal in-plane optical anisotropy in a two-dimensional van der waals crystal. *Nat. Photonics* 1–6 (2024).
42. Xia, M. *et al.* Spectroscopic signatures of AA′ and AB stacking of chemical vapor deposited bilayer MoS_2. *ACS Nano* **9**, 12246–12254 (2015).
43. Zhang, L. *et al.* Tuning electrical conductance in bilayer MoS_2 through defect-mediated interlayer chemical bonding. *ACS Nano* **14**, 10265–10275 (2020).
44. Campanini, M. *et al.* Atomic-resolution differential phase contrast STEM on ferroelectric materials: a mean-field approach. *Phys. Rev. B* **101**, 184116 (2020).
45. Shibata, N. *et al.* Differential phase-contrast microscopy at atomic resolution. *Nat. Phys.* **8**, 611–615

(2012).

46. Abdelwahab, I. *et al.* Giant second-harmonic generation in ferroelectric $NbOI_2$. *Nat. Photonics* **16**, 644–650 (2022).
47. Zhao, L. *et al.* Probing anisotropic deformation and near-infrared emission tuning in thin-layered InSe crystal under high pressure. *Nano Lett.* acs.nanolett.3c00593 (2023).
48. Fan, Y. *et al.* Hidden structural phase transition assisted ferroelectric domain orientation engineering in $Hf_{0.5}Zr_{0.5}O_2$ films. *Nat. Commun.* **16**, 4232 (2025).
49. Mu, X. *et al.* Polarization switching of HfO_2 ferroelectric in bulk and electrode/ferroelectric/electrode heterostructure. *npj Comput. Mater.* **11**, 1–8 (2025).
50. Xia, J. *et al.* Pressure-induced phase transition in weyl semimetallic WTe_2. *Small* **13**, 1701887 (2017).
51. Fu, T. *et al.* Manipulating peierls distortion in van der waals NbOX2 maximizes second-harmonic generation. *J. Am. Chem. Soc.* **145**, 16828–16834 (2023).
52. Li, W. *et al.* Terahertz excitation of collective dynamics of polar skyrmions over a broad temperature range. *Nat. Phys.* 1–8 (2025).
53. Wang, C., Chen, D., Wang, Y. & Meng, S. Directional pumping of coherent phonons and quasiparticle renormalization in a dirac nodal-line semimetal. *Phys. Rev. X* **15**, 021053 (2025).
54. Duan, S. *et al.* Optical manipulation of electronic dimensionality in a quantum material. *Nature* **595**, 239–244 (2021).
55. Ilyas, B. *et al.* Terahertz field-induced metastable magnetization near criticality in FePS3. *Nature* **636**, 609–614 (2024).
56. Basini, M. *et al.* Terahertz electric-field-driven dynamical multiferroicity in SrTiO3. *Nature* **628**, 534–539 (2024).
57. Sie, E. J. *et al.* An ultrafast symmetry switch in a weyl semimetal. *Nature* **565**, 61–66 (2019).
58. Momma, K. & Izumi, F. VESTA 3 for three-dimensional visualization of crystal, volumetric and morphology data. *J. Appl. Crystallogr.* **44**, 1272–1276 (2011).
59. Seto, Y. & Ohtsuka, M. ReciPro: free and open-source multipurpose crystallographic software integrating a crystal model database and viewer, diffraction and microscopy simulators, and

diffraction data analysis tools. *J. Appl. Crystallogr.* **55**, 397–410 (2022).

60. Koch, Christoph T. Determination of core structure periodicity and point defect density along dislocations. (Arizona State University, 2002).
61. Zhang, Q., Zhang, L. Y., Jin, C. H., Wang, Y. M. & Lin, F. CalAtom: a software for quantitatively analysing atomic columns in a transmission electron microscope image. *Ultramicroscopy* **202**, 114–120 (2019).
62. Liu, X.-L., Zhang, X., Lin, M.-L. & Tan, P.-H. Different angle-resolved polarization configurations of raman spectroscopy: a case on the basal and edge plane of two-dimensional materials*. *Chin. Phys. B* **26**, 067802 (2017).
63. Toby, B. H. & Von Dreele, R. B. GSAS-II: the genesis of a modern open-source all purpose crystallography software package. *J. Appl. Crystallogr.* **46**, 544–549 (2013).
64. Kresse, G. & Furthmüller, J. Efficient iterative schemes for ab initio total-energy calculations using a plane-wave basis set. *Phys. Rev. B* **54**, 11169–11186 (1996).
65. Giannozzi, P. *et al.* QUANTUM ESPRESSO: a modular and open-source software project for quantum simulations of materials. *J. Phys.: Condens. Matter* **21**, 395502 (2009).
66. Perdew, J. P., Burke, K. & Ernzerhof, M. Generalized gradient approximation made simple. *Phys. Rev. Lett.* **77**, 3865–3868 (1996).
67. Liu, Y. *et al.* Stacking faults enabled second harmonic generation in centrosymmetric van der waals RhI_3. *ACS Nano* **18**, 17053–17064 (2024).
68. Gonze, X. & Lee, C. Dynamical matrices, born effective charges, dielectric permittivity tensors, and interatomic force constants from density-functional perturbation theory. *Phys. Rev. B* **55**, 10355–10368 (1997).
69. Qi, F. *et al.* Breaking 50 femtosecond resolution barrier in MeV ultrafast electron diffraction with a double bend achromat compressor. *Phys. Rev. Lett.* **124**, 134803 (2020).

Acknowledgements

This work was supported by the National Key Basic Research and Development Program of China (Grant Nos. 2024YFA1409100 (J.H.L.) and 2024YFA1408102 (G.W.)), the National Natural Science

Foundation of China (Grant Nos. 52272146 (Y.Li.), 52473302 (J.H.L.), 52301188 (Z.J.G.) 12404017 (G.W.), 12525501 (D.X.), 12304024 (Y.P.Q.), 12461160252 (J.H.L.), U25A20386 (J.H.L.) and T2525009 (J.H.L.)), the Science and Technology Commission of Shanghai Municipality (Grant No. 24LZ1401000 (Y.Q.F.)), Training Program of the Major Research Plan of the National Natural Science Foundation of China (Grant No. 92565109 (Y.Q.F.)), Guangdong Basic Science Foundation (Grant No. 2023B1515120039 (J.H.L.)), the Natural Science Foundation of Guangdong Province, China (Grant No. 2025A1515011998 (G.W.)), Guangdong Provincial Key Laboratory of Advanced Thermoelectric Materials and Device Physics (Grant No. 2024B1212010001 (J.H.L.)), the Shenzhen Science and Technology Program (Grant No. JCYJ2024120212371201 (C.Y.X.)), the China Postdoctoral Science Foundation (Grant No. 2024M754161 (W.H.)), Quantum Science Strategic Special Project (Grant No. GDZX2301006 (J.H.L.)), Shenzhen Municipal Funding Co-construction Program Project (Grant No. SZZX2301004 (J.H.L.)) from the Quantum Science Center of Guangdong-Hong Kong-Macao Greater Bay Area, China. The UED experiment was supported by the Shanghai soft X-ray free-electron laser facility. The authors would like to thank Dr. Zhaoyuan Sun from the Center of Analysis and Measurement at Harbin Institute of Technology for the assistance in the PFM measurements.

Author Contributions

Y.Li., J.R.F. and Y.Q.F. conceived the project. Y.Q.F. and X.Z.S. synthesized the material and carried out structural characterization. G.W. and J.H.L. performed STEM measurements and data analysis. S.G.L. and T.T.L. help the STEM measurements. W.H., G.T. and Y.T.P. performed DFT calculations and analysis. Z.Y.D. help the DFT calculations. J.R.F. perform the PFM measurements. J.R.F., S.M.Z. and Z.J.Y. perform the SHG measurements. J.R.F. perform the *in-situ* spectra measurements under hydrostatic pressure. Y.Liu., J.P.W. and J.J.Z. help the sample preparation and hydrostatic experiments. D.W. and Y.D. perform the hydrostatic pressure XRD measurements. Y.C.S. and Y.K.Y. perform the millimetre-scale hydrostatic pressure experiments. Y.P.Q. and D.X. perform the UED measurements and analyse the data. Y.Q.F., J.W.H., C.Y.X., F.Q.H., J.H.L., Y.Li., Z.J.G., J.Z.W. and L.Z. supervised the project. J.R.F, G.W., Y.P.Q., W.H., Y.Q.F. and Y.Li. wrote the manuscript with comments from all authors.

Competing interests

The authors declare no competing interests.

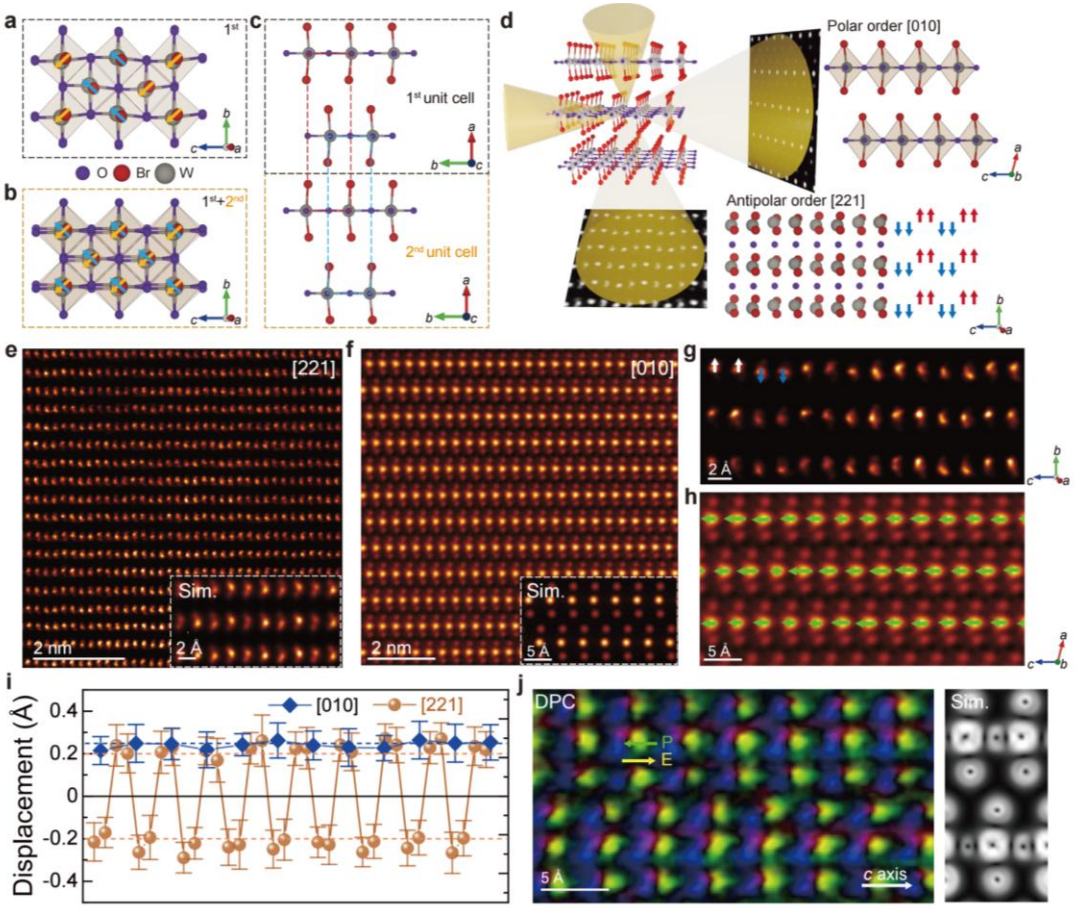

Figure 1. Atomic-scale visualization of noncollinear electric order in few-layer WO_2Br_2. (a, b) Atomic models of WO_2Br_2 with one (a) and two (b) unit cell thicknesses, viewed along the [201] zone axis. Blue and yellow arrows denote the off-centering displacements of W atoms toward the top-left and bottom-left directions, respectively. (c) Side view of AB-stacked in WO_2Br_2, illustrating the alternating orientation of polarization vectors between adjacent layers. (d) Schematic of the 3D projection geometry of the STEM experiment, showing how imaging along the [221] and [201] axes reveal the noncollinear displacements. (e, f) HAADF-STEM images acquired along the [221] (e) and [010] (f) orientations, with insets showing corresponding multi-slice simulation (i.e., Sim.) images. (g, h) High-magnification HAADF-STEM images taken along the [221] (g) and [010] (h) directions, with arrows marking the extracted displacement directions of individual W atoms. (i) Statistical quantification of W-atom displacements along the *b*-axis (from panel e) and the *c*- axis (from panel f), yielding average shifts of ±0.23 Å and ~0.26 Å, respectively (detailed in methods), and data are presented as mean ± SD. Brown and blue short-dashed lines denote the ideal displacements obtained from multi-slice simulations based on the refined atomic structure model (±0.22 Å for [221] and 0.27 Å for [010]). (j) Experimental DPC electric field map and simulated (i.e., Sim.) DPC amplitude of WO_2Br_2 along the [010] orientation, showing an asymmetric atomic electric field distribution caused by the ferroelectric polarization.

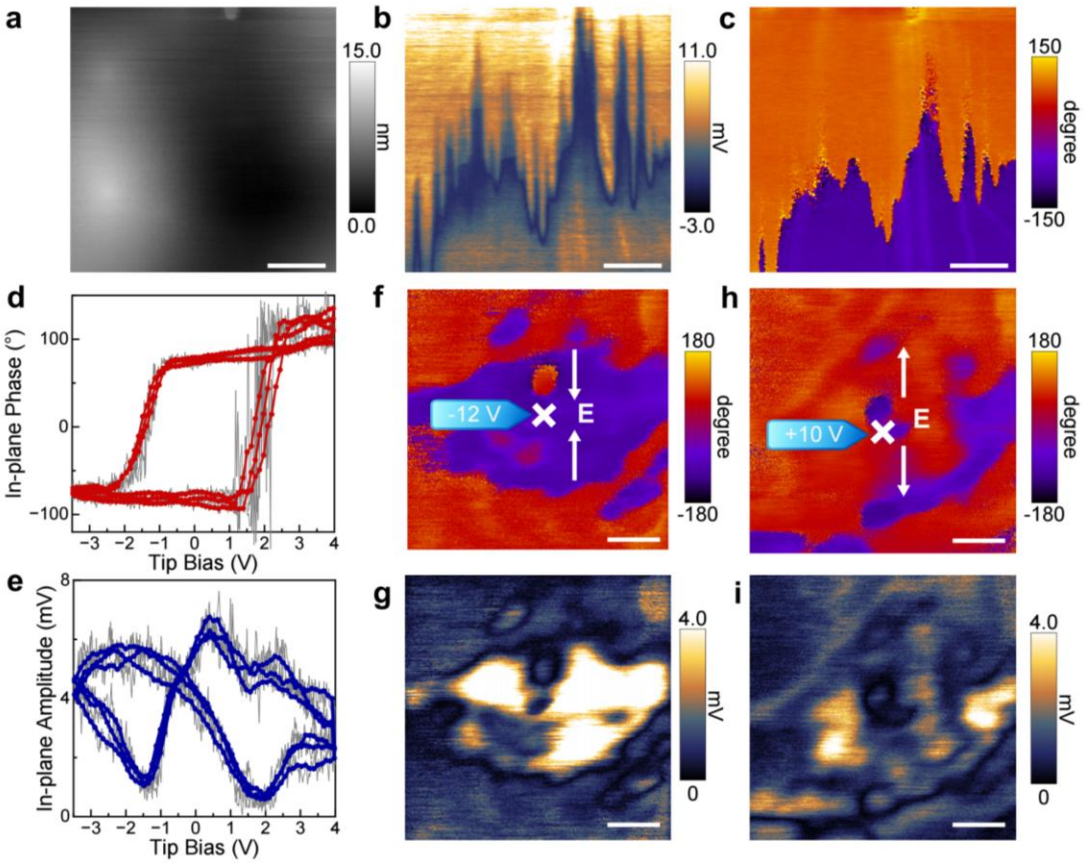

Figure 2. In-plane ferroelectricity in WO_2Br_2. (a) Atomic force microscopy (AFM) topography of an exfoliated WO_2Br_2 nanoflake. (b) PFM in-plane amplitude. (c) The PFM in-plane phase. Scale bar in (a-c) :500 nm. (d, e) Local in-plane PFM phase (d) and amplitude (e) hysteresis loops of WO_2Br_2 nanoflake. The light gray lines represent the original data. (f-i) In-plane phase (f, h) and amplitude (h, i) image after point-voltages were applied on the marked position. The cross symbol marks the location where the tip is positioned for voltage application, and the white arrows indicate the direction of the local electric field. (f, g) -12 V (h, i) +10 V. Scale bar in (f-i): 200 nm.

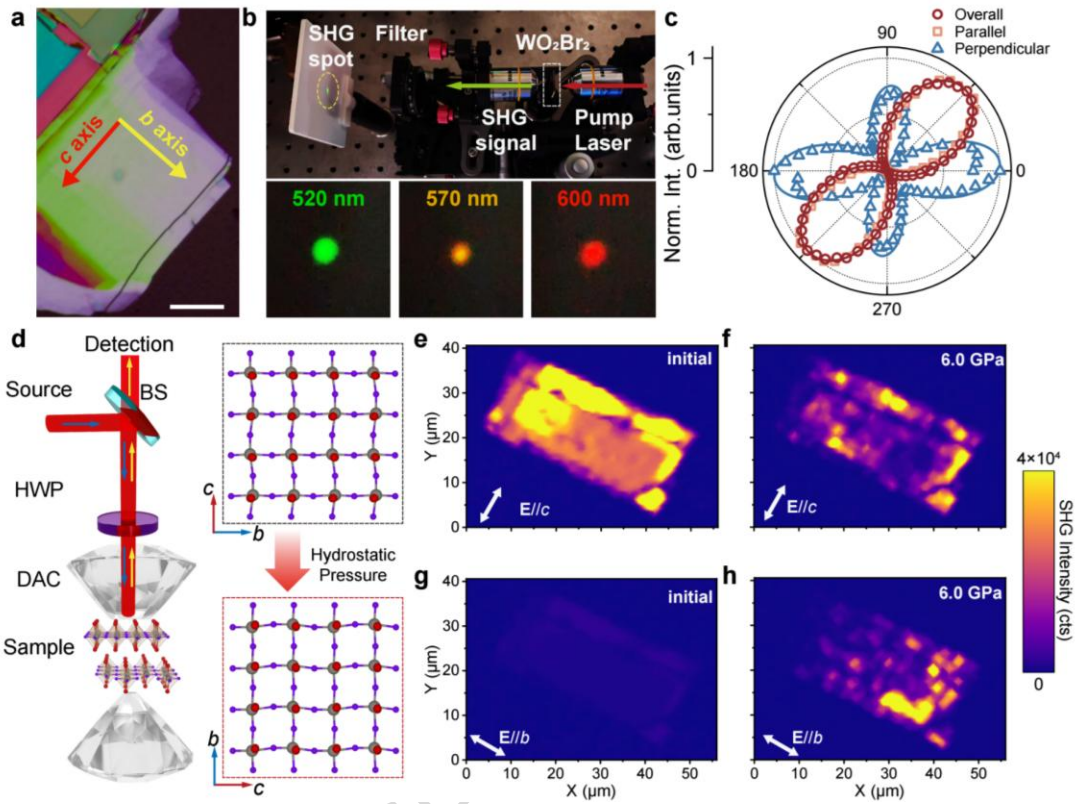

Figure 3. SHG and hydrostatic pressure-induced orientation switching of WO_2Br_2. (a) Optical micrograph of a representative WO_2Br_2 flake for SHG measurement. Scale bar: 20 μm. (b) Optical setup for SHG efficiency measurement (top panel) and panchromatic SHG output under discrete wavelength excitation (520/570/600 nm) (bottom panel). The arrows in top panel indicate the propagation directions of the excitation light and the signal light. (c) Normalized polar plots of SHG intensity versus laser polarization angle under overall (analyzer-free), parallel (analyzer axis parallel to incident polarization), and perpendicular (analyzer axis perpendicular to incident polarization) configurations. Maxima value of each configuration is normalized to unity. The marks represent the original data and the solid lines represent the fitted results. (d) Schematic of crystallographic orientation switching under hydrostatic pressure, where BS means beam splitter, and HWP means half-wave plate. Blue and yellow arrows represent the excitation and the signal light respectively. (e) and (f) SHG intensity mapping of WO_2Br_2 flake under ambient pressure (e) and 6.0 GPa (f), with **E***//c* configuration. (g) and (h) SHG intensity mapping of WO_2Br_2 flake under ambient pressure (g) and 6.0 GPa (h), with **E***//b* configuration. The arrows mean the electric field direction of the excitation light.

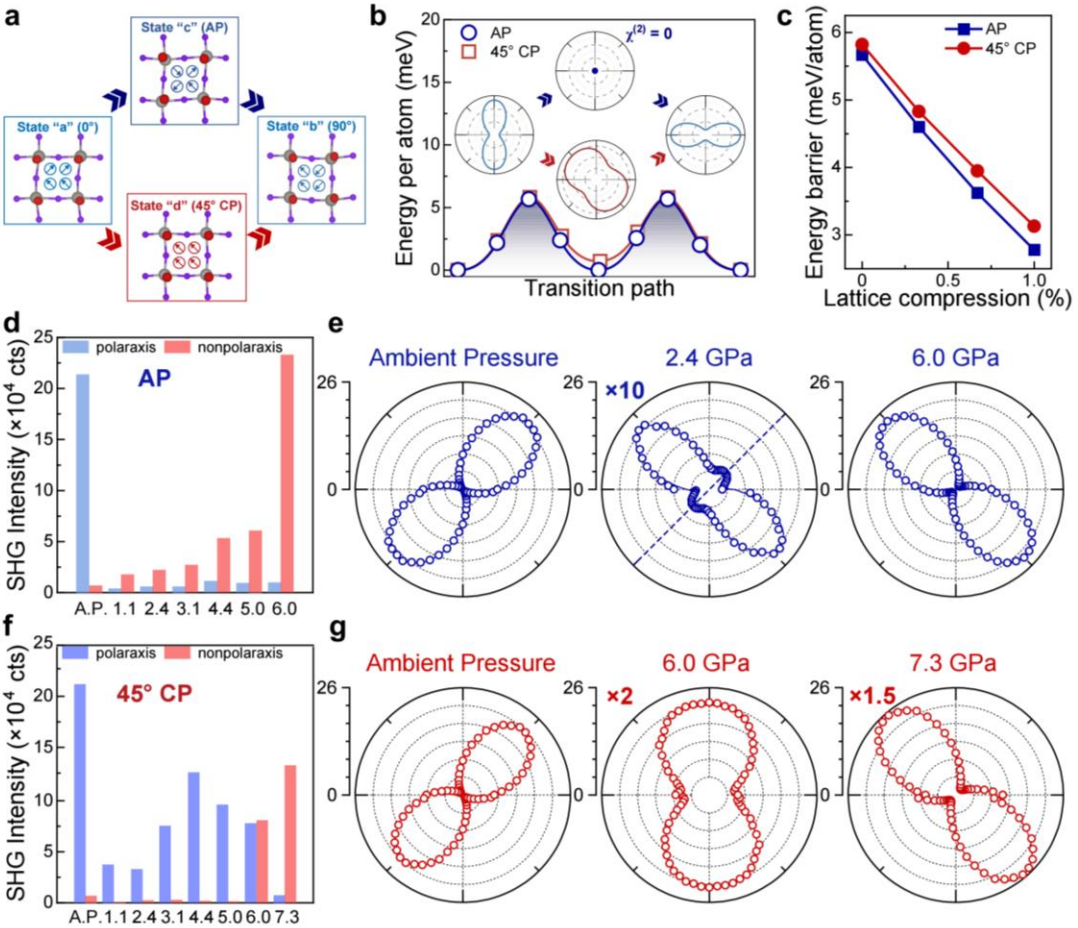

Figure 4. Transition pathways of polarization orientation in WO_2Br_2 under hydrostatic Pressure. (a) Atomic structures of two transition pathways. The arrows show the directions of the local dipoles. (b) Energy transition pathways and SHG polar plots of initial state, intermedium state and final state during the 90° flop of structures. (c) Evolution of energy barriers along the AP and 45° CP pathways under biaxial compressive strain along the *b* and *c* axes. Note that a monolayer model was adopted to be consistent with the NEB calculations, where hydrostatic pressure cannot be applied; therefore, biaxial strain along the *bc* plane was used instead. (d) Pressure-dependent SHG intensity variations along the polar and non-polar axes at ambient pressure, corresponding to the AP transition pathway identified experimentally. A.P. on the axis denotes ambient pressure. (e) SHG polar plots at characteristic pressure points along the AP transition pathway. At 2.4 GPa, the SHG intensity along the polar axis is 1/40 of that at ambient pressure. The dash line represents the pristine polar axis at ambient pressure. (f) Pressure-dependent SHG intensity variations along the polar and non-polar axes at ambient pressure, corresponding to the 45° CP transition pathway identified experimentally. (g) SHG polar plots at characteristic pressure points along the 45° CP transition pathway. The raw data were scaled, and the scaling factors are indicated to the left of the corresponding polar plots for clarity in the SHG polar plots in (e) and (g).

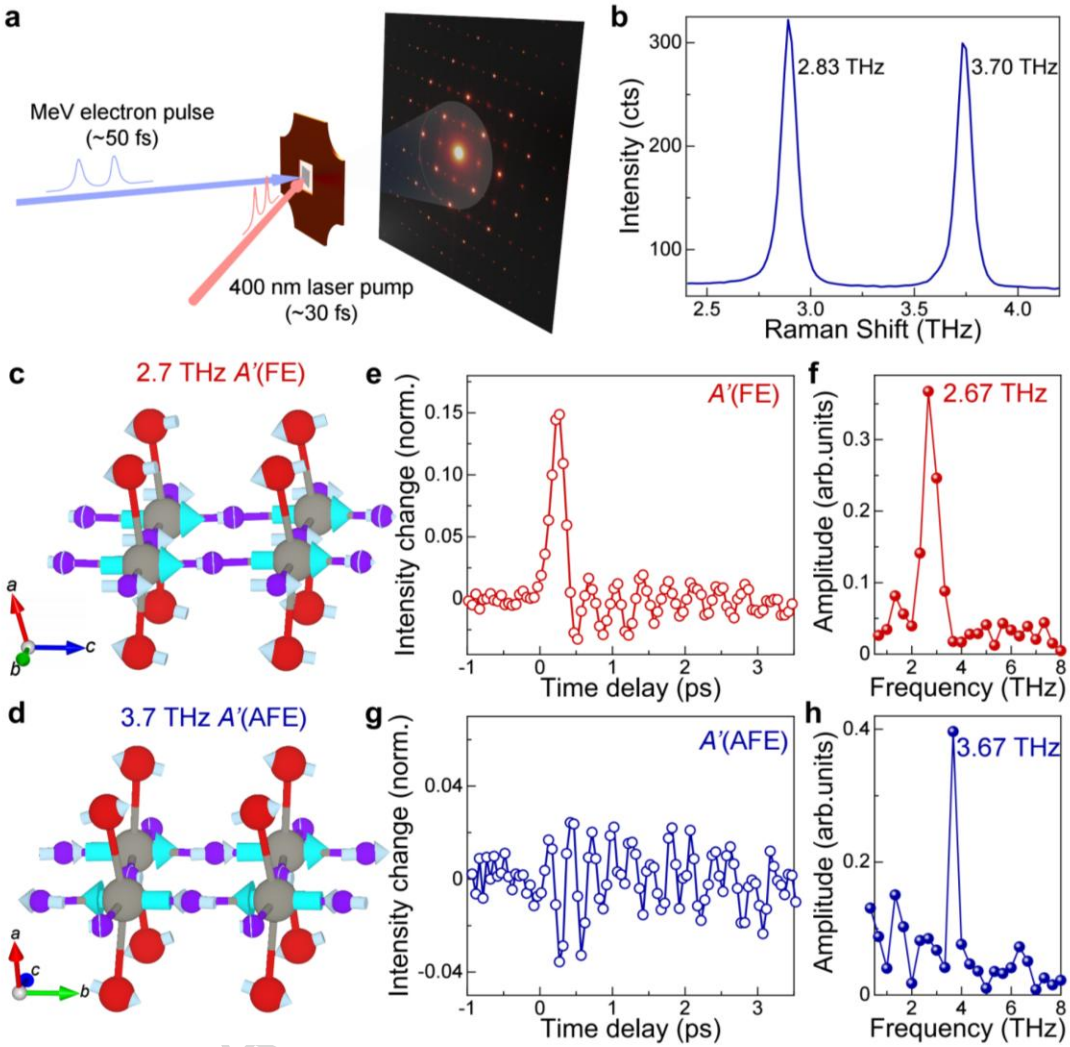

Figure 5. Excitation of the FE and AFE coherent phonon mode. (a) An illustration of the ultrafast electron diffraction experimental setup. (b) Raman spectra exhibits the 2.83 THz and 3.70 THz phonon mode. (c-d) The atomic vibrations acquired by DFT simulation of the 2.70 THz FE phonon mode (c) and the 3.70 THz AFE phonon mode (d). The atomic motions are indicated by arrows with different colors, which were scaled to exhibits the vibration directions clearly. (e-f) Photoexcited coherent FE phonon mode *A'*(FE) with the frequency of 2.70 THz by fast Fourier transformation. (g-h) Photoexcited coherent AFE phonon mode *A'*(FE) with the frequency of 3.70 THz by fast Fourier transformation.

Editor's summary:

The authors reveal intrinsic long-range-order noncollinear electric dipole order in the van der Waals crystal WO_2Br_2, enabling pressure-driven 90° polarization rotation via multiple transition pathways and distinctive ultrafast phonon dynamics.

Peer review information: *Nature Communications* thanks Morgan Trassin and the other anonymous reviewer(s) for their contribution to the peer review of this work. A peer review file is available.